High-order Laguerre-Gauss polychromatic beams from Bragg-Berry flat optics

Mikaël Ghadimi Nassiri,[1] Seong Yong Cho,[2] Hiroyuki Yoshida,[2,3] Masanori Ozaki,[2] and Etienne Brasselet[1,*]

[1]*Université de Bordeaux, CNRS, LOMA, UMR 5798, F-33400 Talence, France*

[2]*Division of Electrical, Electronic and Information Engineering, Graduate School of Engineering, Osaka University, 2-1 Yamada-oka, Suita, Osaka 565-0871, Japan*

[3]*Japan Science and Technology Agency, Precursory Research for Embryonic Science and Technology (JST PRESTO), 4-1-8 Honcho, Kawaguchi, Saitama 332-0012, Japan*

(Received 25 September 2018; published 26 December 2018; corrected 15 November 2019)

We report on the design, fabrication, and experimental characterization of reflective geometric phase optical elements enabling the generation of scalar and vectorial high-order Laguerre-Gauss optical beams over a broad spectral range. This is made possible by combining azimuthal and radial structuring of helix-based liquid-crystal films exhibiting the circular Bragg reflection phenomenon. By extending the previously introduced concept of Bragg-Berry optical elements to the polychromatic shaping of the radial degrees of freedom and showing their combination with azimuthal ones, this work suggests that spectrally broadband spin-orbit processing of optical information over multiple spatial degrees of freedom can be further considered on experimental grounds.

DOI: 10.1103/PhysRevA.98.063834

I. INTRODUCTION

Taming light is at the heart of photonics technologies, which implies the development of optical components enabling agile control of amplitude, phase, and polarization state of light, ideally both in time and space and over a broad spectral range. Despite the development of optical devices with ever-increasing performances, combining all these assets remains an ideal that motivates further researches. Present study takes place in the context of geometric (Berry) phase flat optics made of space-variant optically anisotropic slabs following a concept proposed two decades ago [1]. Usually, practical implementations correspond to transmissive optical elements based on inhomogeneous uniaxial slabs having in-plane two-dimensional distribution of the optical axis orientation denoted by the angle ψ and uniform birefringent phase retardation. Phase shaping of the transmitted light occurs as the polarization (i.e., "spin") and the spatial (i.e., "orbit") degrees of freedom mutually couple through the spin-orbit interaction, as detailed in the review paper [2]. In short, considering an incident circularly polarized light field, the two circularly polarized components of the transmitted field acquire a dynamic phase associated with the average optical thickness of the element while only the contracircularly polarized component picks up an extra geometric phase $\Phi_{\rm geom} = \pm 2\psi$, where the $\pm$ sign refers to the handedness of the incident circular polarization state. As its name suggests, the key feature of the latter phase change is that it is solely coded into the geometry of the material structure while the birefringent phase retardation merely dictates the fraction η of the output photons that are spin-flipped and geometric-phase shaped. A noticeable consequence is the achromatic nature of the spatially modulated phase, which is an asset for the emergence of broadband spin optics.

However, the drawback of the above-mentioned geometric phase elements is that they operate efficiently only for a discrete set of wavelengths $\{\lambda_i\}$ for which the birefringent phase retardation Δ satisfies the "half-wave plate condition" $\Delta(\lambda_i) = (2n+1)\pi$ (n integer), hence $\eta(\lambda_i) = 1$. Several approaches have been discussed to circumvent this practical issue by exploiting the third spatial dimension. This is done by breaking the translational invariance of the permittivity tensor along the propagation direction of light [3–7]. Indeed, this allows us to partly compensate for the intrinsic dispersion of the birefringent phase retardation of a material, as early explored in the 1950s in the case of non-space-variant birefringent retarders [8–10]. In 2016, it was proposed to use helix-based modulation of the permittivity tensor to create geometric phase mirrors operating over a large spectral bandwidth, using spatially patterned chiral liquid crystal (cholesteric) slabs for experimental demonstrations [11–15]. The idea consists of combining the naturally broadband reflective half-wave plate behavior associated with the circular Bragg reflection of chiral anisotropic media [16] with the spatial modulation of the Berry phase via in-plane modulation of the helix azimuthal positioning. The latter is described by the liquid-crystal molecular orientation angle ψ at the boundaries of the cholesteric slab of thickness L, as sketched in Fig. 1. We refer to the introductory section of Ref. [17] for a generic presentation of such "Bragg-Berry" optical elements.

Since early experimental demonstrations of beam shaping capabilities (deflection, lensing, vortex generation) using cholesterics-based Bragg-Berry flat optics [11–15] and the understanding of the geometrical nature of the phenomenon [13,15], several following studies explored various facets of the possibilities offered by this approach. In particular, the concept was extended to other chiral mesophases such as cholesteric blue phases that are chiral liquid crystals with three-dimensional periodicity [18]. Other demonstrations include spin-controlled wide-angle diffuse reflection from

*etienne.brasselet@u-bordeaux.fr

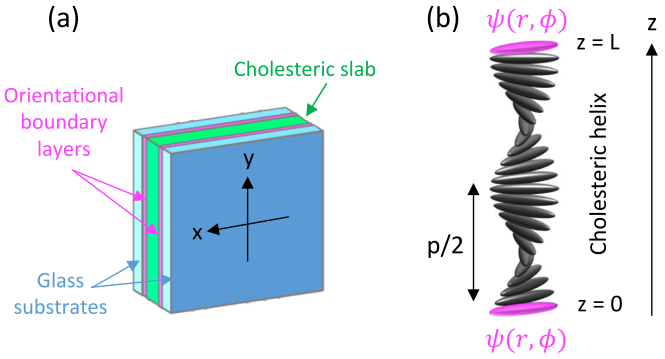

FIG. 1. (a) Illustration of our Bragg-Berry optical elements made of a cholesteric liquid-crystal film sandwiched between glass substrates provided with identical photopatterned orientational boundary layers. (b) Sketch of the helical ordering of the liquid-crystal molecules along the normal to the plane of the film, here in the case of a right-handed cholesteric. Note that the drawing is not on scale since in practice $L/p \sim 30$.

random patterns [19], spin-controlled holography [20], and spin-controlled digital optics [21]. Clearly, state-of-the-art liquid-crystal patterning techniques [22,23] now allow considering Bragg-Berry reflectors having arbitrary optical functionalities. On the other hand, developments made in the optics of cholesterics towards circular photonic band-gap broadening and polarization independent reflective behavior [24] have been generalized to the space-variant case. Namely, the fabrication of gradient-pitch ultrabroadband (i.e., with a bandwidth of several hundreds of nanometers) Bragg-Berry optical elements [17,25] as well as spin-independent highly reflective devices [26] have been reported.

Specifically, spin-to-orbital optical angular momentum mapping ensured by geometric phase optical elements satisfying the half-wave plate condition presents a large set of promising applications in the classical and quantum regimes that has been recognized several years ago [27] and the deployment of versatile technologies remains an open issue with a lot of technical and conceptual expectations [28]. In this framework, here we aim at exploring the ability of Bragg-Berry optical elements to shape polychromatic fundamental Gaussian modes into arbitrary Laguerre-Gauss modes that form an orthogonal basis for the scalar paraxial Helmholtz equation [29], each mode being associated with two indices. Namely, the azimuthal index $l \in \mathbb{Z}$ proportional to the orbital angular momentum carried by photon [30] and the radial index $p \in \mathbb{N}$ that refers to the number of nodes of the wave function along the radial coordinate ($r > 0$). Note that these two independent transverse degrees of freedom provide an attractive basis for the optical information that could add to wavelength and spin channels. Also, previous Bragg-Berry demonstrations were restricted so far to Laguerre-Gauss modes with fundamental radial order $p = 0$ [12–14,17,21,25,26]. Therefore, using p as an additional degree of freedom, the present study suggests that spectrally broadband spin-orbit processing of optical information over multiple spatial degrees of freedom can be further considered on experimental grounds. Moreover, polychromatic high-order vectorial Laguerre-Gauss beams constructed from the coherent superposition of orthogonally polarized scalar beams are obtained, which generalizes previously discussed spin-to-orbital angular momentum mapping [26] by adding another independent transverse spatial degree of freedom.

II. PREPARATION OF THE BRAGG-BERRY OPTICAL ELEMENTS

A. Paraxial design

At first, we recall the electric-field complex amplitude of a Laguerre-Gauss beam with indices (l, p) and waist radius w in its focal plane. Namely, up to an unimportant prefactor,

$$E_{l,p}(r,\phi) = \left(\frac{r}{w}\right)^{|l|} L_p^{|l|}\left(\frac{2r^2}{w^2}\right) \exp\left(-\frac{r^2}{w^2} + il\phi\right), \quad (1)$$

where (r, ϕ) are the usual polar coordinates in the transverse plane and $L_p^{|l|}(X) = \sum_{k=0}^{p} \frac{(|l|+p)!}{(|l|+k)!(p-k)!k!}(-X)^k$ refers to the generalized Laguerre polynomials. Of course, ideal Laguerre-Gauss beam shaping from an incident fundamental Gaussian beam with planar wave front ($l = 0$, $p = 0$) by using a two-dimensional transfer function implies both amplitude and phase spatial modulation. Dealing here with optical elements designed to operate with a spectrally flat maximal reflectance, our approach consists of encoding the information on l as a continuous linear azimuthal structuring of the orientational boundary layer while the information on p is encoded as a discrete set of radial structural jumps. Namely,

$$\psi_{l,p}(r,\phi) = \frac{l}{2}\phi + \left\{1 - \mathrm{sgn}\left[L_p^{|l|}\left(\frac{2r^2}{W^2}\right)\right]\right\}\frac{\pi}{4}, \quad (2)$$

where $\mathrm{sgn}(X)$ refers to the sign of X and the distance W is the radial design parameter. In that case, the geometric phase $\pm 2\psi_{l,p}(r,\phi)$ acquired by the Bragg-reflected circular component (which corresponds to cohanded electric and material helices) is that of a Laguerre-Gauss field with azimuthal index $\pm l$, radial index p, and waist W. This option is a standard one in the context of high-order Laguerre-Gauss beam generated by phase-only spatial modulation [31–33], though other phase-only options have also been developed [34–37]. Still, there is always a compromise between the purity of the generated mode and the efficiency of the process, which always makes the use of a given approach open to debate.

Here, the chosen orientational design given by Eq. (2) implies to find the ratio between the incident Gaussian beam waist, w_{in} and the design parameter W that optimizes the output modal content. The latter is evaluated in the far field from the projection coefficient $c_{l,p}$ of the output far field on the far field of a Laguerre-Gauss beam with indices (l, p), which is given by

$$c_{l,p} = \frac{\int_0^{2\pi}\int_0^{\infty} \widetilde{E}_{\mathrm{out}}\widetilde{E}_{l,p}^{*}\,\kappa d\kappa d\theta}{\sqrt{\int_0^{2\pi}\int_0^{\infty} |\widetilde{E}_{\mathrm{out}}|^2\kappa d\kappa d\theta \int_0^{2\pi}\int_0^{\infty} |\widetilde{E}_{l,p}|^2\kappa d\kappa d\theta}}, \quad (3)$$

where $\widetilde{F}(\kappa,\theta) = \int_0^{2\pi}\int_0^{\infty} F(r,\phi)\exp[-i\kappa r(\cos\theta\cos\phi + \sin\theta\sin\phi)]r dr d\phi$ is the Fourier transform of the function $F(r,\phi)$ and the asterisk denotes complex conjugation. Noting that when $F(r,\phi) = \mathcal{F}(r)e^{im\phi}$ the Fourier transform simplifies to $\widetilde{F}(\kappa,\theta) = 2\pi(-i)^m e^{im\theta}\widehat{\mathcal{F}}(\kappa)$ where

TABLE I. Optimal values of the modal purity for the first high-order Laguerre-Gauss modes.

$\eta_{l,p}^{\mathrm{opt}}$	$l=0$	$l=1$	$l=2$
$p=1$	0.817	0.825	0.804
$p=2$	0.778	0.785	0.778
$p=3$	0.758	0.763	0.761

TABLE II. Optimal values of the ratio w_{in}/W for the first high-order Laguerre-Gauss modes.

$(w_{\mathrm{in}}/W)^{\mathrm{opt}}$	$l=0$	$l=1$	$l=2$
$p=1$	1.73	1.97	2.17
$p=2$	2.17	2.35	2.52
$p=3$	2.55	2.67	2.84

$\widehat{\mathcal{F}}(\kappa)=\int_0^\infty \mathcal{F}(r)J_m(\kappa r)rdr$ is the Hankel transform and J_m is the mth-order Bessel function of the first kind, the fraction of the total output power carried by the mode (l,p) in the far field, $\eta_{l,p}=\eta_{-l,p}=|c_{l,p}|^2$, simplifies to

$$\eta_{l,p}=\frac{\left|\int_0^\infty \widehat{\mathcal{E}}_{\mathrm{out}}\widehat{\mathcal{E}}_{l,p}^{*}\kappa d\kappa\right|^2}{\int_0^\infty |\widehat{\mathcal{E}}_{\mathrm{out}}|^2\kappa d\kappa\int_0^\infty |\widehat{\mathcal{E}}_{l,p}|^2\kappa d\kappa}. \tag{4}$$

The sought-after design thus corresponds to the optimization of the modal purity $\eta_{l,p}$ with respect to the two independent parameters w_{in}/W and w, recalling that the dependence on w is associated to the fact that the decomposition of a paraxial light field on the Laguerre-Gauss basis is not unique [38,39]. Using $E_{\mathrm{out}}=\exp[-r^2/w_{\mathrm{in}}^2\pm 2i\psi_{l,p}(r,\phi)]$ we calculate the optimal values $\eta_{l,p}^{\mathrm{opt}}$ for $l=(0,1,2)$ and $p=(1,2,3)$, which are reported in Table I. The corresponding values for the experimental parameter w_{in}/W are presented in Table II.

B. Fabrication

The photopatterned samples as sketched in Fig. 1(a) were prepared from glass substrates with 2 cm × 1.5 cm that are single-side spin coated (at 500 rpm for 5 s followed by 4000 rpm for 30 s) with a photoalignment agent (LIA-03, from DIC). Then, the substrates are assembled using a photocurable adhesive (NOA68T, from Norland) and calibrated spacers into a plane-parallel cell with a 9-μm gap. The orientational pattern is photoinscribed simultaneously on the two inner sides on the cell by using a projection exposure setup made of a linearly polarized liquid-crystal display projector having 1024 × 768 pixels (ELP-820, from Epson), a bandpass filter at 436 nm wavelength and 10 nm bandwidth, a motorized half-wave plate, and relay optics. The cell is sequentially irradiated over a 3.43-mm × 2.57-mm area by light patterns whose linear polarization state direction dictates the alignment orientation, that are mutually perpendicular. The pixel size of the recorded structure therefore corresponds to 3.3 μm, however, because the photoalignment layer cannot be developed like a photoresist and the liquid-crystal orientation changes continuously on a substrate, the achieved effective resolution is expected to be less. Still, the quality of the recorded structures is high enough to ensure the fabrication of clean photonic functionalities, as reported here.

Since w_{in}/W is fixed by design (Table II), the finite size of the sample imposes a tradeoff for the choice of the incident beam waist. If the latter is too large, the multizone pattern for ψ does not fit the alignment area whereas if it is too small, the gradients of ψ are not resolved at the photoinscription step. Practically, w_{in} is chosen as a fourth of the smallest dimension of the rectangular photoaligned layer and we measure $w_{\mathrm{in}}=655$ μm. The corresponding ψ map given by Eq. (2) is shown in the left part of each panel in Fig. 2. Another practical constraint is associated with the irradiation duration needed to ensure proper photoalignment. This led us to use a discretized design made of contiguous sectors having a 10° angular increment for ψ along the azimuthal coordinate; see the right part of each panel in Fig. 2. Each sector being irradiated during 5 min, the whole process takes 10 min for $l=0$ and 90 min for $l\geqslant 1$.

Towards an experimental demonstration in the visible domain, we use a cholesteric liquid crystal prepared by doping the achiral nematic material MLC-2140 (from Merck) with the left-handed chiral molecular dopant S-5011 (from Merck) with the wt % proportions (97.3 : 2.7). This gives a circular photonic band gap around 530 nm; see the reflectance spectra shown in Fig. 3 for an incident circularly polarized light field whose electric-field helix has the same handedness as that of the cholesteric helix, which corresponds to the Bragg reflection condition. High-order Laguerre-Gauss Bragg-Berry optical components are then obtained by capillary filling the cells with the cholesteric mixture in the isotropic phase—namely, at 100 °C whereas the clearing point of MLC-2140

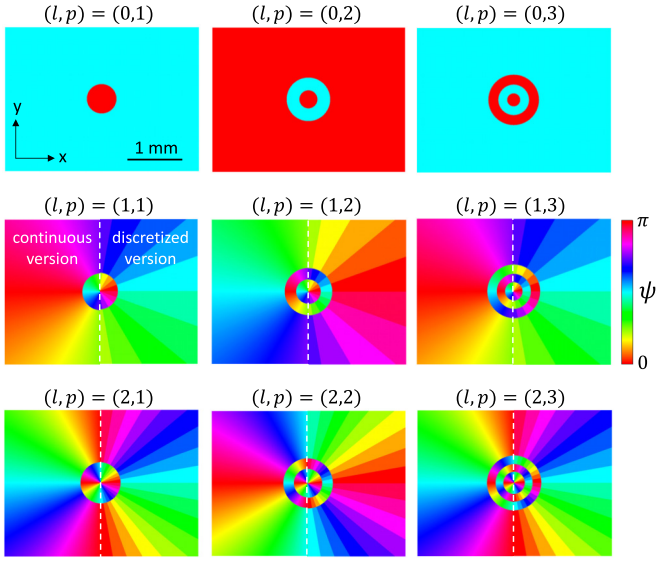

FIG. 2. Maps of the orientational boundary conditions for $l=(0,1,2)$ and $p=(1,2,3)$ given by the optimized design procedure described in the text. The right part of each panel (except for $l=0$) displays the fabricated discretized version while the left part refers to the continuous ideal version given by Eq. (2). The shown area actually corresponds to the structured area of the fabricated samples.

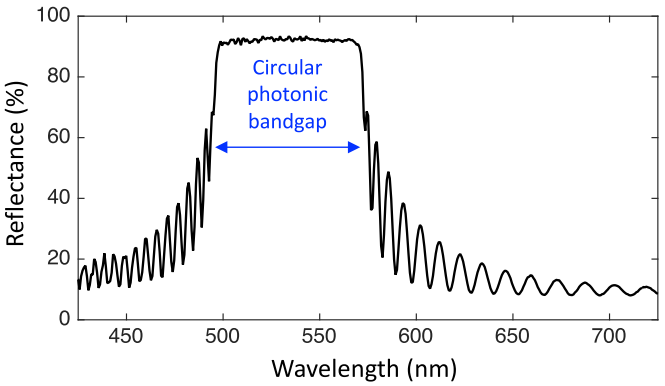

FIG. 3. Typical reflectance spectrum of a sample recorded at normal incidence using an incident circularly polarized light that is cohanded with the cholesteric helix. The corresponding circular photonic band gap has a spectral width of approximately 70 nm.

is at 88 °C—followed by slow cooling down to room temperature at 0.3 °C min $^{-1}$.

C. Structural characterization

The orientational structure of fabricated optical elements is characterized by interferometry. This is done by replacing one of the two mirror of a Michelson interferometer by the sample and observing the fringes located at the input facet of the sample. The results are shown in Fig. 4 when the light source is an halogen lamp spectrally filtered at 532 nm using a bandpass filter with a bandwidth of 10 nm and left circularly polarized using a linear polarizer and an achromatic quarter-wave plate.

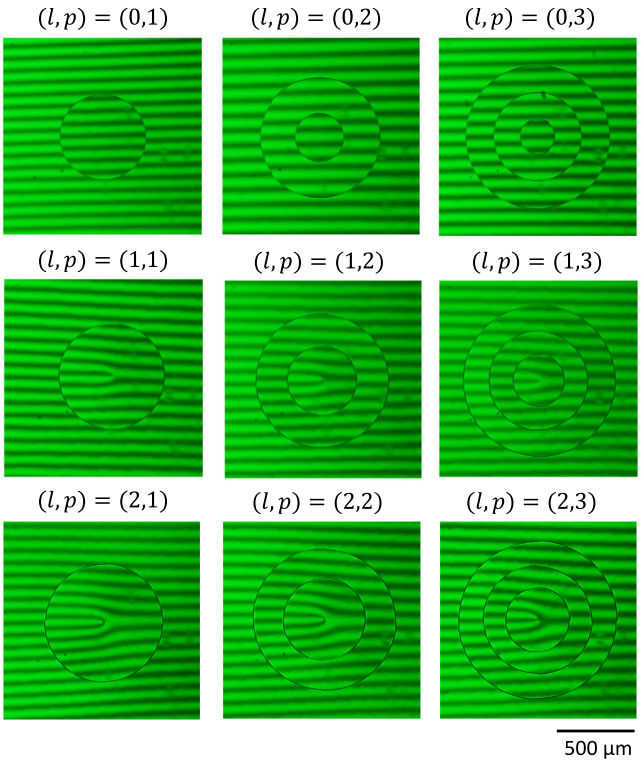

FIG. 4. Interferogram in the plane of the sample obtained at 532-nm wavelength obtained from a Michelson interferometer by using the Bragg-Berry optical element as one of the two mirrors of the interferometer for $l = (0, 1, 2)$ and $p = (1, 2, 3)$.

Both the radial index p and the azimuthal index l can be assessed from the interferograms. Indeed, p is the number of dark circles that refers to the zeros of the function $L_p^{|l|}(2r^2/W^2)$. The latter are associated with a $\pi/2$ jump for the angle ψ, hence high local gradients for the molecular orientation leading to strong light scattering. The width δr of these disordered rings between adjacent regions having distinct azimuthal orientation for the cholesteric helix is measured by collecting the data for all the fabricated samples and we find $\delta r = 9.2 \pm 1.9$ μm. The corresponding π geometric phase jump can be grasped by looking at half-fringe jumps on the interferograms. On the other hand, l is the number of extra fringes forming the forked intensity pattern associated with an optical phase singularity with topological charge l.

III. HIGH-ORDER LAGUERRE-GAUSS BEAM SHAPING

A. Far-field optical characterization

Beam shaping capabilities of our elements are tested using the setup sketched in Fig. 5, where the light source is a laser source at 532-nm wavelength and a lens is used to image the far field by placing it in a $2f$ configuration with respect to the sample and the camera in order to perform optical Fourier transform with the lens. The Bragg-reflected field at normal incidence is recorded on a camera, taking care to suppress the unavoidable unwanted Fresnel reflection from the input air-glass interface of the element. This is done by preparing a linearly polarized incident polarization state and selecting the orthogonal polarization state for the observations. In that case, the polarization-preserved Fresnel reflection is therefore blocked by the output polarizer while there is always a contribution of the circularly polarized Bragg-reflected light that passes through the output polarizer.

As shown in Fig. 6, the incident Gaussian beam is shaped into an intensity profile that qualitatively possesses all the expected attributes. Namely, there are p circles with null intensity and on-axis intensity is null when $l \neq 0$ as expected from the presence of an optical phase singularity. These features are retrieved in the far-field fringe pattern obtained by superimposing a coherent Gaussian reference beam; see Fig. 7. Indeed, both the topological charge of the on-axis singularity and the oscillating electric-field amplitude (i.e., the π phase jump associated with location of null intensity) can

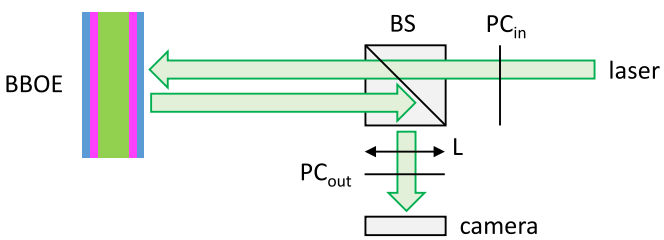

FIG. 5. Experimental setup for far-field optical characterization. BBOE: Bragg-Berry optical element; BS: beamsplitter; L: lens; PC_{in} and PC_{out}: input and output polarization controller.

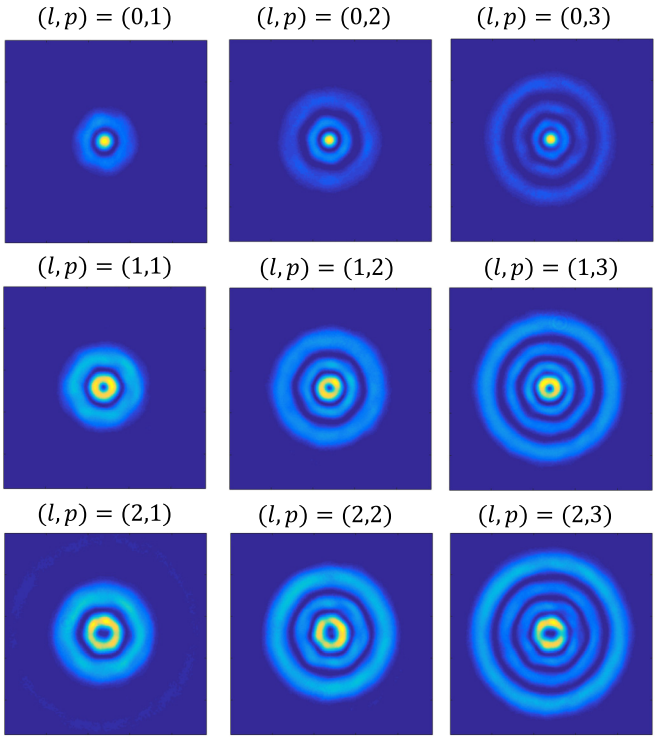

FIG. 6. Far-field intensity patterns reflected off the Bragg-Berry optical elements for $l = (0, 1, 2)$ and $p = (1, 2, 3)$. Here the light source is a supercontinuum laser spectrally filtered at 532 nm with a 10-nm bandwidth.

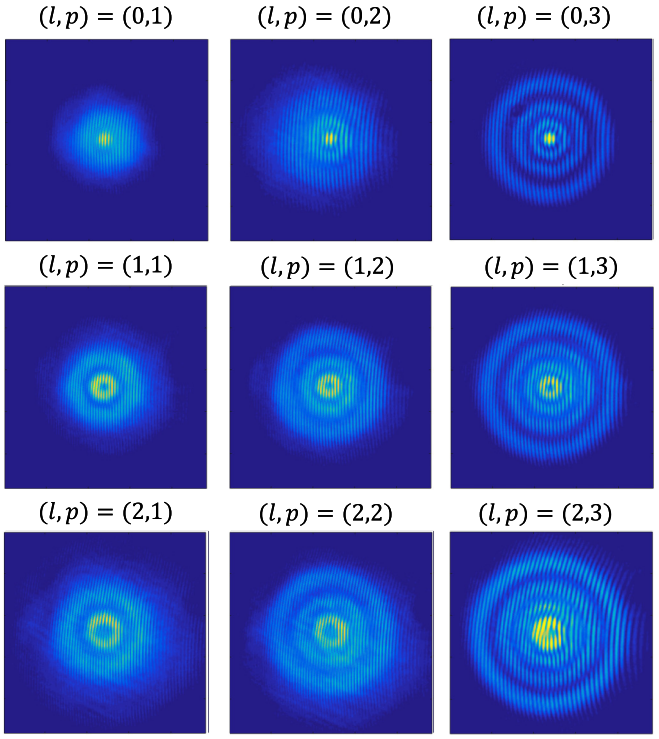

FIG. 7. Fringe patterns obtained from the interference of the far field reflected off the Bragg-Berry optical elements for $l = (0, 1, 2)$ and $p = (1, 2, 3)$. The light source is the same as in Fig. 6.

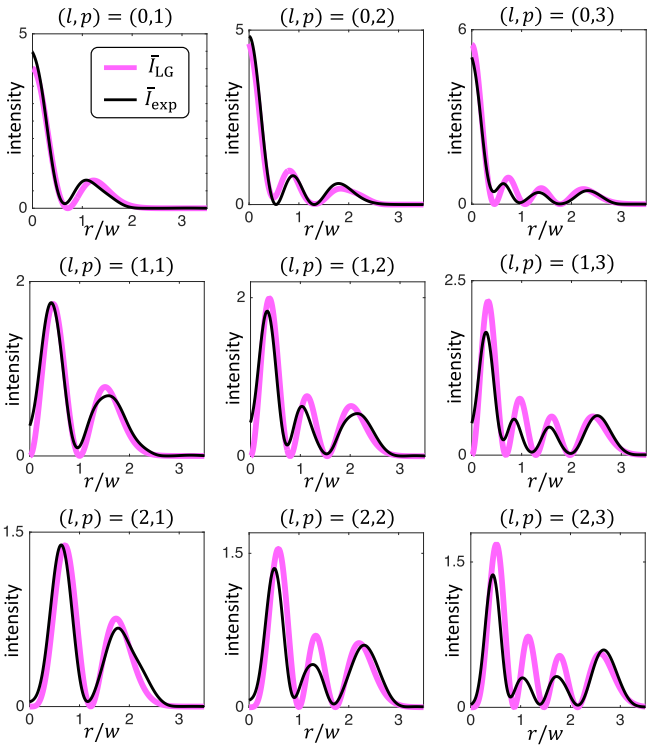

FIG. 8. Radial dependence of the normalized far-field intensity patterns, $\bar{I} = I/\sqrt{\int_0^{2\pi}\int_0^{\infty} I^2 r dr d\phi}$, for $l = (0, 1, 2)$ and $p = (1, 2, 3)$. Thin curves: experiment. Thick curves: Laguerre-Gauss (LG) fit using the estimator given by Eq. (5).

be easily grasped. More quantitatively, Laguerre-Gauss beam shaping is assessed by maximizing the overlap integral $\zeta_{l,p}$ between the experimental (I_{exp}) and expected ($I_{l,p} \propto |E_{l,p}|^2$) intensity profiles according to

$$\zeta_{l,p} = \frac{\int_0^{2\pi}\int_0^{\infty} I_{\text{exp}} I_{l,p} r dr d\phi}{\sqrt{\int_0^{2\pi}\int_0^{\infty} I_{\text{exp}}^2 r dr d\phi \int_0^{2\pi}\int_0^{\infty} I_{l,p}^2 r dr d\phi}}, \quad (5)$$

where the waist parameter w in $I_{l,p}$, see Eq. (1), is the only adjustable parameter. The results are shown in Fig. 8, which exhibits an overall fair agreement.

B. Spin-to-orbital angular momentum mapping

As recalled in the Introduction, a major asset of transmissive geometric phase optical elements developed so far is that they enable the mapping of two-dimensional orbital angular momentum subspaces from two-dimensional spin angular momentum basis at a given wavelength. The latter feature is a consequence of the spin-controlled reversal of the geometric phase. In the case of Bragg-Berry optical elements, the polychromatic benefit however comes with a major drawback, since the geometric phase reversal is lost using an element as described in Fig. 1(a). Indeed, the reflective beam shaping is only achieved for cohanded electric and material helices. Still, this constraint is released by adding a standard rear mirror, as demonstrated in a recent work [26] in the case of optical vortex generation.

Applying this recipe, we obtain high-order Laguerre-Gauss modes with spin-controlled azimuthal index, as illustrated

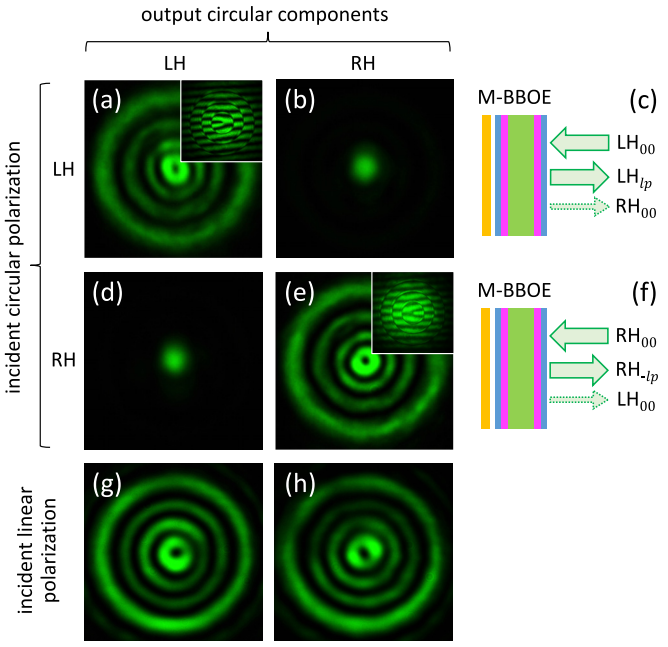

FIG. 9. Left-handed (LH) and right-handed (RH) output circular components in the case of a mirror-backed Bragg-Berry optical element (M-BBOE) for LH circular (a),(b), RH circular (d),(e), and linear (g),(h) incident polarization state, here for $(l, p) = (1, 3)$ and recalling that we use a left-handed cholesteric liquid crystal. These results are obtained by proper setting of the input and output polarization controllers as shown in Fig. 5. The light source is the same as in Fig. 6 for incident LH and RH circular polarization state whereas a continuous-wave diode-pumped solid-state laser at 532 nm is used for incident linear polarization state in order to preserve the temporal coherence between the two circular components. The sketches on the right part (c),(f) illustrate the spin-dependent azimuthal index of the generated high-order Laguerre-Gauss beam. This is experimentally identified by looking at the Michelson fringe pattern, as shown in the inset panels for LH-LH and RH-RH cases.

in the first two rows of Fig. 9 in the case $(l, p) = (1, 3)$, by placing a standard mirror at $\sim$1 mm from the back side of the Bragg-Berry element. Indeed, a left-handed circularly polarized incident field, $\mathbf{E}_{\text{in}} \propto (\mathbf{x} + i\mathbf{y})/\sqrt{2}$, generates a left-handed Laguerre-Gauss beam with indices (l, p) as light is reflected off the front side of the structured cholesteric layer, see Fig. 9(a), as discussed in the previous section. On the other hand, a right-handed circularly polarized incident field, $\mathbf{E}_{\text{in}} \propto (\mathbf{x} - i\mathbf{y})/\sqrt{2}$, is not Bragg-reflected by the front side of the optical element but nevertheless generates a right-handed Laguerre-Gauss beam with indices $(-l, p)$ as light is reflected off the element; see Fig. 9(e). In that case, beam shaping can be understood according to the following ray-optics reasoning. At first, the incident beam propagates through the cholesteric and is reflected by the rear mirror. Since the latter flips the circular polarization handedness, the field then acquires its geometric phase spatial modulation as it is Bragg reflected by the back side of the structured cholesteric film, towards the rear mirror. The circular polarization handedness is therefore flipped one more time by the rear mirror and the structured light eventually passes through the optical element and exits.

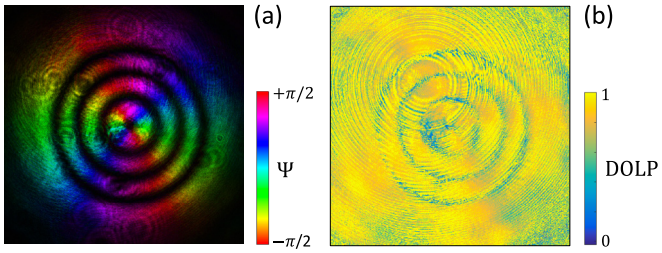

FIG. 10. Characterization of the high-order Laguerre-Gauss vector beam generated by a mirror-backed Bragg-Berry optical elements with $(l, p) = (1, 3)$. (a) Measured intensity and polarization state azimuth to the total reflected field in the case of incident linear polarization state. The luminance refers to the intensity and the color map refers to the azimuth angle, $\Psi = \frac{1}{2}\arctan(s_2/s_1)$. (b) Degree of linear polarization, $\text{DOLP} = \sqrt{s_1^2 + s_2^2}$. In the latter expressions $s_{1,2}$ refers to the usual reduced Stokes parameters.

These two situations are respectively sketched in Figs. 9(c) and 9(f), which also display the residual fraction of the incident light that is not structured; see Figs. 9(b) and 9(e). Indeed, in practice the circular Bragg phenomenon is not associated with an ideal 100% reflectance; see Fig. 3. Therefore, any Bragg reflected light experiencing geometric phase shaping is associated with a small fraction of unstructured light, which adds to the residual unstructured contribution arising from Fresnel reflections at air-glass interfaces.

Note that the situation is similar for a Bragg-Berry optical element prepared from a right-handed cholesteric, for which one only needs to account for the change RH $\leftrightarrow$ LH and $l \leftrightarrow -l$ in Fig. 9 while keeping the same orientational pattern given by Eq. (2).

From the superposition principle, the total reflected field in the case of incident linear polarization is the sum of equal weights high-order Laguerre-Gauss beams having orthogonal circular polarization state, opposite l and identical p, as shown in Figs. 9(g) and 9(h). Such a field refers to a high-order Laguerre-Gauss vector beam characterized by an inhomogeneously linearly polarized field with azimuthally varying polarization state azimuth angle Ψ that winds l times per full rotation around the propagation axis. The latter characteristics are experimentally assessed by Stokes polarimetric imaging [40]; see Fig. 10, where the data for the intensity and polarization azimuth are combined in panel (a). On-axis vector point singularity with Poincaré-Hopf index l [41] is actually observed. In addition, the degree of linear polarization in everywhere close to the ideal unit value; see Fig. 10(b).

C. Broadband features

Although experimental data presented above are all made at 532-nm wavelength, which is approximately in the center of the circular photonic band gap (Fig. 3), one can easily extend obtained results to a polychromatic field, as demonstrated in earlier works on optical vortex generation [12,14,17,26]. This is done here for the sake of illustration in the case of high-order Laguerre-Gauss beam generation with $(l, p) = (1, 3)$ under cohanded incident circular polarization without rear mirror, by using a supercontinuum laser source and a

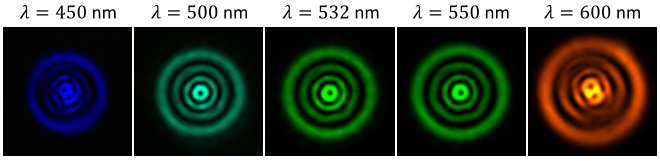

FIG. 11. Experimental set of spectral components for the far-field intensity profiles of the generated high-order Laguerre-Gauss beam by a Bragg-Berry optical element with $(l, p) = (1, 3)$. The displayed wavelengths refer to the central wavelength of bandpass filter with 10 nm bandwidth. The acquisition and exposure time depends on the wavelength to exploit the full dynamic range of the used eight-bit camera.

set of interferential filters. Observations are made between crossed linear polarizers in order to minimize the effect of Fresnel reflections. Still as the amount of Bragg-reflected light decreases outside the band gap, the effect of all residual mismatches come at play. This leads to nontrivial interference patterns, as shown in Fig. 11 at 450- and 600-nm wavelengths for which a pair of vector point singularities with half-integer Poincaré-Hopf index are revealed by the output polarizer.

IV. CONCLUSION

Summarizing, we have extended previous development of Bragg-Berry optical elements to the generation of a spin-orbit optical basis in the paraxial regime based on both azimuthal and radial spatial degrees of freedom for polychromatic light. The present demonstration made in the visible domain using helix-based liquid crystals with space-variant rotational positioning of the supramolecular helices could be extended to other frequency domains. In particular, the near-infrared domain could be accessible by mere detuning of the cholesteric pitch. One can also mention the recent demonstration of Bragg-Berry concept in the microwave domain using metallic helices [42], which invite us to design and test other options such as microfabricated solid-state options that could be used in the terahertz domain.

Finally, recalling recent advances in the fabrication of chiral materials endowed with photoactivity at the molecular scale [43], spin-orbit photonics based on chiral materials may reveal itself as a powerful strategy to manipulate multiple degrees of freedom of a light field (polarization, space, frequency, time) at once with a single device.

ACKNOWLEDGMENTS

This study has been carried out with financial support from the French National Research Agency (Project No. ANR-15-CE30-0018), DGA, Conseil Régional d'Aquitaine, JST PRESTO (JPMJPR151D) and JSPS KAKENHI (Grant No. 17H02766). The authors thank DIC for providing the photoalignment material.

[1] R. Bhandari, Polarization of light and topological phases, Phys. Rep. **281**, 1 (1997).
[2] K. Y. Bliokh, F. J. Rodríguez-Fortuño, F. Nori, and A. V. Zayats, Spin-orbit interactions of light, Nat. Photon. **9**, 796 (2015).
[3] C. Oh and M. J. Escuti, Achromatic diffraction from polarization gratings with high efficiency, Opt. Lett. **33**, 2287 (2008).
[4] Y. Li, J. Kim, and M. J. Escuti, Broadband orbital angular momentum manipulation using liquid crystal thin films, SPIE Proc. **8274**, 827415 (2012).
[5] R. K. Komanduri, K. F. Lawler, and M. J. Escuti, Multi-twist retarders: Broadband retardation control using self-aligning reactive liquid crystal layers, Opt. Express **21**, 404 (2013).
[6] N. V. Tabiryan, S. V. Serak, S. R. Nersisyan, D. E. Roberts, B. Y. Zeldovich, D. M. Steeves, and B. R. Kimball, Broadband waveplate lenses, Opt. Express **24**, 7091 (2016).
[7] N. Tabirian, H. Xianyu, and E. Serabyn, High efficiency broadband liquid crystal polymer vector vortex waveplates, in *2017 IEEE Aerospace Conference* (IEEE, Big Sky, MT, USA, 2017), pp. 1–7.
[8] G. Destriau and J. Prouteau, Réalisation d'un quart d'onde quasi achromatique par juxtaposition de deux lames cristallines de même nature, J. Phys. Radium **10**, 53 (1949).
[9] S. Pancharatnam, Achromatic combinations of birefringent plates. Part I. An achromatic circular polarizer, Proc. - Indian Acad. Sci., Sect. A **41**, 130 (1955).
[10] S. Pancharatnam, Achromatic combinations of birefringent plates. Part II. An achromatic quarter-wave plate, Proc. Indian Acad. Sci. A **41**, 137 (1955).
[11] J. Kobashi, H. Yoshida, and M. Ozaki, Planar optics with patterned chiral liquid crystals, Nat. Photon. **10**, 389 (2016).
[12] J. Kobashi, H. Yoshida, and M. Ozaki, Polychromatic Optical Vortex Generation from Patterned Cholesteric Liquid Crystals, Phys. Rev. Lett. **116**, 253903 (2016).
[13] M. Rafayelyan, G. Tkachenko, and E. Brasselet, Reflective Spin-Orbit Geometric Phase from Chiral Anisotropic Optical Media, Phys. Rev. Lett. **116**, 253902 (2016).
[14] M. Rafayelyan and E. Brasselet, Bragg-Berry mirrors: Reflective broadband q-plates, Opt. Lett. **41**, 3972 (2016).
[15] R. Barboza, U. Bortolozzo, M. G. Clerc, and S. Residori, Berry Phase of Light Under Bragg Reflection by Chiral Liquid-Crystal Media, Phys. Rev. Lett. **117**, 053903 (2016).
[16] M. Faryad and A. Lakhtakia, The circular Bragg phenomenon, Adv. Opt. Photon. **6**, 225 (2014).
[17] M. Rafayelyan, G. Agez, and E. Brasselet, Ultrabroadband gradient-pitch Bragg-Berry mirrors, Phys. Rev. A **96**, 043862 (2017).
[18] H. Yoshida and J. Kobashi, Flat optics with cholesteric and blue phase liquid crystals, Liq. Cryst. **43**, 1909 (2016).
[19] Y. Mohri, J. Kobashi, H. Yoshida, and M. Ozaki, Morpho-butterfly-inspired patterning of helical photonic structures for circular-polarization-sensitive, wide-angle diffuse reflection, Adv. Opt. Mater. **5**, 1601071 (2017).
[20] J. Kobashi, H. Yoshida, and M. Ozaki, Circularly-polarized, semitransparent and double-sided holograms based on helical photonic structures, Sci. Rep. **7**, 16470 (2017).
[21] P. Chen, L.-L. Ma, W. Duan, J. Chen, S.-J. Ge, Z.-H. Zhu, M.-J. Tang, R. Xu, W. Gao, T. Li, W. Hu, and Y.-Q. Lu,

Digitalizing self-assembled chiral superstructures for optical vortex processing, Adv. Mater **30**, 1705865 (2018).

[22] J. Kim, Y. Li, M. N. Miskiewicz, C. Oh, M. W. Kudenov, and M. J. Escuti, Fabrication of ideal geometric-phase holograms with arbitrary wavefronts, Optica **2**, 958 (2015).

[23] W. Ji, C.-H. Lee, P. Chen, W. Hu, Y. Ming, L. Zhang, T.-H. Lin, V. Chigrinov, and Y.-Q. Lu, Meta-q-plate for complex beam shaping, Sci. Rep. **6**, 25528 (2016).

[24] M. Mitov, Cholesteric liquid crystals with a broad light reflection band, Adv. Mater. **24**, 6260 (2012).

[25] J. Kobashi, H. Yoshida, and M. Ozaki, Broadband optical vortex generation from patterned cholesteric liquid crystals, Mol. Cryst. Liq. Cryst. **646**, 116 (2017).

[26] M. Rafayelyan and E. Brasselet, Spin-to-Orbital Angular Momentum Mapping of Polychromatic Light, Phys. Rev. Lett. **120**, 213903 (2018).

[27] L. Marrucci, E. Karimi, S. Slussarenko, B. Piccirillo, E. Santamato, E. Nagali, and F. Sciarrino, Spin-to-orbital conversion of the angular momentum of light and its classical and quantum applications, J. Opt. **13**, 064001 (2011).

[28] H. Rubinsztein-Dunlop, A. Forbes, M. V. Berry, M. R. Dennis, D. L. Andrews, M. Mansuripur, C. Denz, C. Alpmann, P. Banzer, T. Bauer *et al.*, Roadmap on structured light, J. Opt. **19**, 013001 (2017).

[29] A. E. Siegman, *Lasers* (University Science Books, Mill Valley, 1986).

[30] L. Allen, M. W. Beijersbergen, R. J. C. Spreeuw, and J. Woerdman, Orbital angular momentum of light and the transformation of Laguerre-Gaussian laser modes, Phys. Rev. A **45**, 8185 (1992).

[31] Y. Ohtake, T. Ando, N. Fukuchi, N. Matsumoto, H. Ito, and T. Hara, Universal generation of higher-order multiringed Laguerre-Gaussian beams by using a spatial light modulator, Opt. Lett. **32**, 1411 (2007).

[32] G. Ruffato, M. Massari, and F. Romanato, Generation of high-order Laguerre–Gaussian modes by means of spiral phase plates, Opt. Lett. **39**, 5094 (2014).

[33] P. Chen, B.-Y. Wei, W. Ji, S.-J. Ge, W. Hu, F. Xu, V. Chigrinov, and Y.-Q. Lu, Arbitrary and reconfigurable optical vortex generation: A high-efficiency technique using director-varying liquid crystal fork gratings, Photon. Res. **3**, 133 (2015).

[34] S. Khonina, V. V. Kotlyar, R. Skidanov, V. Soifer, P. Laakkonen, and J. Turunen, Gauss-Laguerre modes with different indices in prescribed diffraction orders of a diffractive phase element, Opt. Commun. **175**, 301 (2000).

[35] V. Arrizón, U. Ruiz, R. Carrada, and L. A. González, Pixelated phase computer holograms for the accurate encoding of scalar complex fields, J. Opt. Soc. Am. A **24**, 3500 (2007).

[36] T. Ando, Y. Ohtake, N. Matsumoto, T. Inoue, and N. Fukuchi, Mode purities of Laguerre-Gaussian beams generated via complex-amplitude modulation using phase-only spatial light modulators, Opt. Lett. **34**, 34 (2009).

[37] S. Ngcobo, I. Litvin, L. Burger, and A. Forbes, A digital laser for on-demand laser modes, Nat. Commun. **4**, 2289 (2013).

[38] C. Schulze, S. Ngcobo, M. Duparré, and A. Forbes, Modal decomposition without a priori scale information, Opt. Express **20**, 27866 (2012).

[39] G. Vallone, Role of beam waist in Laguerre-Gauss expansion of vortex beams, Opt. Lett. **42**, 1097 (2017).

[40] M. S. Soskin, V. G. Denisenko, and R. I. Egorov, Singular stokes-polarimetry as new technique for metrology and inspection of polarized speckle fields, in *Optical Micro-and Nanometrology in Manufacturing Technology* (International Society for Optics and Photonics, Strasbourg, France, 2004), Vol. 5458, pp. 79–86.

[41] I. Freund, Polarization singularity indices in Gaussian laser beams, Opt. Commun. **201**, 251 (2002).

[42] C. Fang, C. Wu, Z. Gong, S. Zhao, A. Sun, Z. Wei, and H. Li, Broadband and high-efficiency vortex beam generator based on a hybrid helix array, Opt. Lett. **43**, 1538 (2018).

[43] A. Ryabchun and A. Bobrovsky, Cholesteric liquid crystal materials for tunable diffractive optics, Adv. Opt. Mater. **6**, 1800335 (2018).

Correction: Terms containing ratios in Sec. II and Table II contained typographical errors and have been fixed.